YINSAR: a Compact, Low-Cost Synthetic Aperture Radar

Douglas G. Thompson, Adam E. Robertson, David V. Arnold, David G. Long
Brigham Young University
459 CB, Provo, UT 84602
voice: 801-378-4884, FAX: 801-378-6586, e-mail: thompsod@ee.byu.edu

Abstract—

Synthetic Aperture Radar (SAR) has proven useful for many different applications. Many more applications would be possible with a low-cost instrument. To address this need, BYU has developed its interferometric SAR, YINSAR. This compact, low-cost system is operated from a four passenger aircraft. This paper reports the current status of YINSAR. We report the results of some new theoretical work and empirical tests regarding the performance of interferometric SAR. We show data collected with the YINSAR hardware empirically verifying the theoretical statistics of interferograms and estimate the accuracy and sensitivity of this instrument. We describe a new method of combining interferograms from multiple baselines to reduce the error in the final height map.

INTRODUCTION

In recent years, Synthetic Aperture Radar (SAR) images have been used in many different fields of study. One such field is archaeology. Several researchers [1, 2, 3] have used spaceborne SAR in a remote survey of the Taklamakan desert of China. They were able to see features such as waterways, ancient ruins, and sections of the Great Wall of China. Blom et al [4] and others have shown that SAR images can help in the detection of ancient roads. Another application is geology. Zebker and Rosen [5] used ERS-1 SAR data in differential interferometric mode to map the coseismic displacement fields resulting from a major earthquake, achieving sub-centimetric accuracy in displacement.

Many other applications of SAR are possible with appropriate instruments. For example, interferometric or differential interferometric SAR could be used to monitor the motion of a landslide by making periodic measurements. A mining company could use interferometric SAR to estimate the volume of material removed from a site. Power plants could use interferometric SAR to estimate the volume of coal reserves on hand. Detailed archaeological surveys of small areas can be performed to assist the archaeologists in making site maps and locating promising dig locations. Such applications require a SAR with low operating costs to give wide access to the scientific community. A compact SAR which is mounted in a small airplane would be well suited for these applications and others.

To address the need for such a SAR, Brigham Young University has developed YSAR [6] and YINSAR. These are compact, inexpensive instruments designed to be flown in four or six passenger aircraft. The cost and complexity are kept low through the use of an all-digital IF and by using commercially available parts for most components. The original system, YSAR, was a prototype which showed the feasibility of small SAR. YINSAR is an interferometric system built on the experience gained from YSAR. Many aspects of the system have been improved. YSAR is now being rebuilt and integrated with the YINSAR system to benefit from these improvements and create a dual-frequency system.

This paper reports the current state of YINSAR and shows new results in IFSAR performance design and analysis. The following section discusses the YINSAR and some of the technological advances which have made it possible. The following section discusses the experiments we have performed with YINSAR hardware which confirm the theoretical statistics of interferograms, as well as estimating the statistics of YINSAR. The next section describes a new method of combining interferograms from multiple baselines to create a height map with less error than a single baseline can give.

YINSAR

YINSAR is an interferometric system based in part on the YSAR design [6]. The block diagram is shown in Fig. 1. The custom RF subsystem was built with special care to improve robustness and signal-to-noise ratio. The motion measurement and compensation system combines differential GPS with high-accuracy inertial measurement. A micro-controller unit controls subsystem power supplies, thus reducing the load when not collecting data. The entire system is controlled through a graphical interface on a laptop computer. This interface includes a map to assist in navigation and to help guide the pilot onto the desired flight path.

The YINSAR instrument resides in three $17 \times 19 \times 7$ inch ($43 \times 48 \times 18$ cm) rack-mountable boxes which could easily be stacked in the space of a single passenger seat. These boxes respectively contain the computer, the RF/IF subsystem and system controller, and the motion measurement subsystem. The system consumes approximately 600 W in full-power operation. The transmitter is 10 W. The antennas are horns fed by a slotted waveguide array. The 10-slot array forms the beam in the azimuth direction, and the horn forms the beam in the range direction. The beamwidths are 9 and 40 degrees in azimuth and range respectively. The current interferometric baseline is approximately one meter and near horizontal. In the future, we plan to add additional receive antennas to implement the multi-baseline techniques described below.

The resolution of the interferometric images is expected to be better than a meter in all three directions. Range resolution will be on the order of a meter. Resolution in azimuth and in elevation should be a half meter or better. This system is currently in the final stages of ground testing. While we had hoped to have images at the time of publication, these were not available due to development delays.

ESTIMATING THE INTERFEROMETRIC ACCURACY

In this section we consider the interferometric accuracy and sensitivity of SAR systems and of YINSAR in particular. We show measurements using the YINSAR hardware which verify theoretical statistics of interferograms, and estimate the accuracy and sensitivity for YINSAR using actual system parameters.
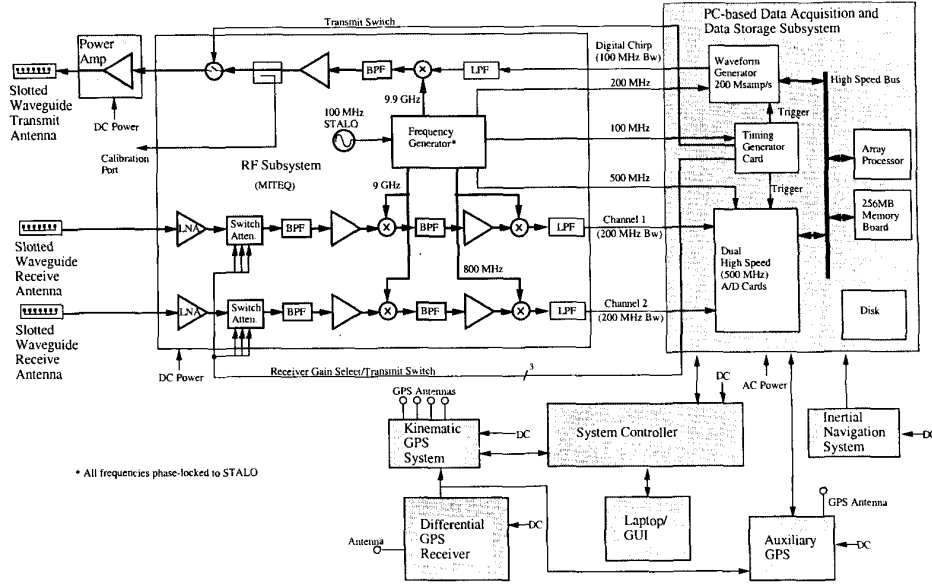
Figure 1: YINSAR Block Diagram

Just and Bamler [7] show that the probability distribution function of the interferometric phase difference, ϕ, is,

$$\text{pdf}(\phi) = \frac{1 - |\gamma|^2}{2\pi} \frac{1}{1 - |\gamma|^2 \cos^2(\phi - \phi_o)} \times$$
$$\left\{ 1 + \frac{|\gamma| \cos(\phi - \phi_o) \cos^{-1}[-|\gamma| \cos(\phi - \phi_o)]}{[1 - |\gamma|^2 \cos^2(\phi - \phi_o)]^{1/2}} \right\}, (1)$$

where ϕ is the phase difference of the interferometric pair, γ is the complex correlation coefficient, and ϕ_o is defined by,

$$\phi_o = \arg\{\gamma\}. \tag{2}$$

The correlation coefficient can be calculated from the data as $|\gamma|$. The pdf of Eq. (1) is periodic in 2π. pdf(ϕ) vs ϕ for several values of $|\gamma|$ is plotted in Fig. 2. The pdf converges to a delta function as $|\gamma|$ approaches unity, and is a uniform distribution for $|\gamma| = 0$. Figure 3 shows the experimentally determined probability distribution function. The plots come from over 10^4 phase measurements taken by YINSAR as the SNR was varied from zero to 20 dB. Both receive channels of YINSAR were connected to the same RF signal source and the signal power was varied to give different signal-to-noise ratios and correlation coefficients. The mean was subtracted from the data to center it at $\phi = 0$. Figure 4 shows the theoretical and empirically measured results of Figs. 2 and 3 together. The pdfs are in excellent agreement, verifying the accuracy of Eq. (1).

The standard deviation σ_ϕ of ϕ can be calculated as in Just and Bamler's work. This value is dependent solely on the phase and the correlation coefficient of the data. γ, the total correlation coefficient, has three components: thermal noise, spatial decorrelation, and temporal decorrelation, and can be written as

$$\gamma = \rho_{spatial} \cdot \rho_{thermal} \cdot \rho_{temporal} \tag{3}$$

Assuming that the SNR for the two returns are identical the decorrelation due to thermal effects is [8, 9],

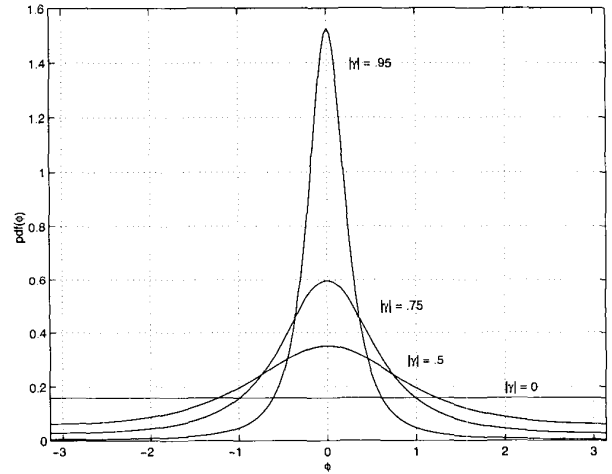$$\rho_{thermal} = \frac{1}{1 + SNR^{-1}}. \tag{4}$$

Figure 2: As the correlation coefficient approaches unity, pdf(θ) approaches a delta function. For a completely uncorrelated signal, $\gamma = 0$, the distribution is uniform. (Adapted from [7]).

The phase standard deviation vs signal to noise ratio is plotted in Fig. 5 using Eq. (4) where $\rho_{spatial}$ and $\rho_{temporal}$ are assumed to have unity value. Empirical measured results from YINSAR are compared to the theoretical values and are in agreement. As expected, the phase standard deviation is highly dependent on the signal to noise ratio.

Using the YINSAR radar parameters, the noise-equivalent σ_0 has been estimated at 35 dB. According to [10], most terrain has σ_0 in the range of about -15 to -5 dB, corresponding to a YINSAR signal to noise ratio of 20 to 30 dB. The estimated values for the sensitivity λ^* and for the standard deviation of the height σ_h for these two values as a function of baseline length
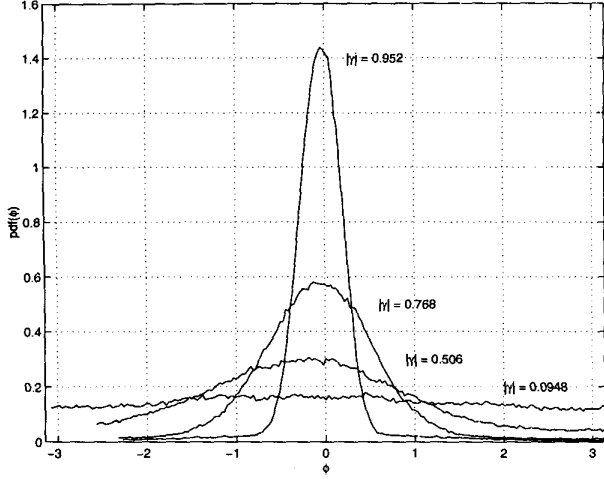
Figure 3: Empirically measured probability distribution function of the phase. Each measurement of γ used 10^4 samples. The mean was subtracted from the data to center it at $\phi = 0$.
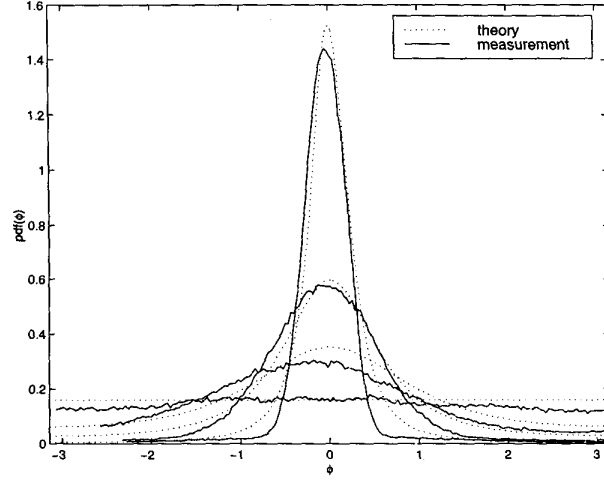

Figure 4: The theoretical and empirically measured results of Figs. 2 and 3 compared. The pdfs are in excellent agreement.

are plotted in Fig. 6. The accuracy can be seen to be as low as 20 cm for the high range of signal-to-noise ratios with a 1-m baseline.

MULTI-BASELINE INTERFEROMETRY

We are developing new techniques in multi-baseline interferometry which we plan to apply to YINSAR. These techniques will greatly minimize the phase unwrapping process and errors resulting from that process. We start by estimating the height from a small baseline, then use that estimate in an iterative process to determine the phase wraps for the larger baselines. We thus gain the higher accuracy of the large baseline with few of the problems created by the greater phase wrapping. A simulated urban scene is used to illustrate the effectiveness of the multi-baseline technique.
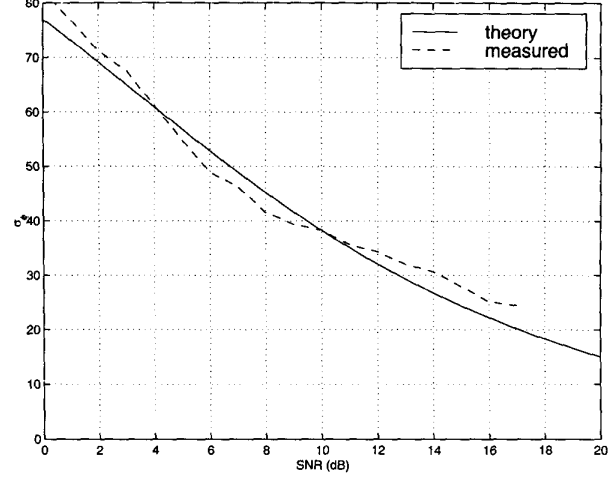
Figure 5: The phase standard deviation, σ_ϕ, vs SNR. Spatial and temporal correlation are assumed unity. The phase standard deviation falls offs sharply with the signal to noise ratio. Empirical measurements made with YINSAR are in agreement with the theoretical values.
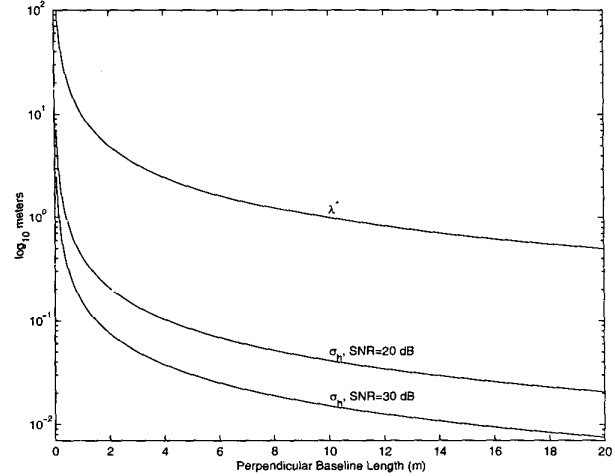

Figure 6: Sensitivity, λ^* and height standard deviation, σ_h, vs. perpendicular baseline length, $B_\perp$ for an incidence angle of $\theta = 45°$. The best (lowest) height sensitivity and standard deviation are achieved for longer baseline lengths.

Our multi-baseline technique [12] is iterative in that we first estimate the height map using a small baseline. We then proceed to larger baselines, each time using the previous estimate only to determine phase wraps. The choice of baseline sizes is based on meeting a criterion for probability of error in the phase wraps of the next step. The final product combines the accuracy of the large baseline with the continuity of the small baseline. The phase-unwrapping errors which occur in this process tend to propogate through the iterations and become worse, so either a median or a mean filter is used between each step.

A synthetic urban scene is illustrated in Fig. 7. Georectification and the removal of the nominal flat earth induced phase
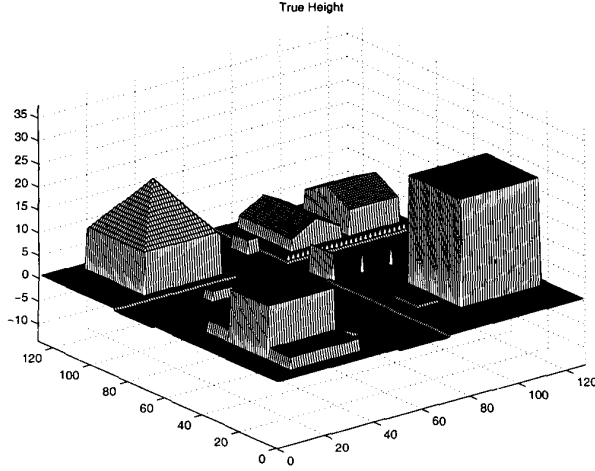
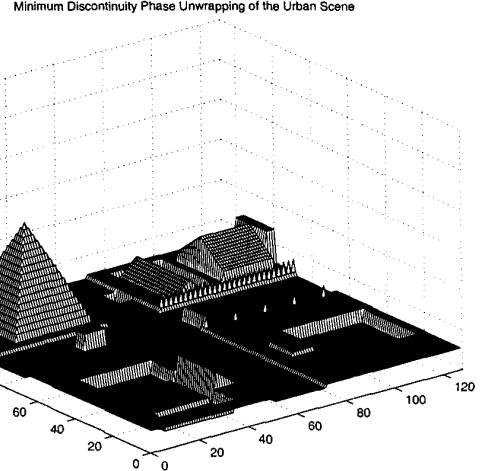Figure 7: True Height of the Simulated Urban Scene

Figure 8: Height estimate of an urban scene using a single interferometric baseline and Flynn's minimum discontinuity phase unwrapping method. For simplicity, noiseless phase measurements were used. Phase unwrapping assumes any step discontinuity to have a magnitude of less than λ^*.

difference are assumed. It is also assumed that data with an SNR of 10 dB is available at all points in the image. The examples shown here assume the imaging geometry given in Table 1, similar to that of YINSAR.

Table 1: Interferometric Imaging Geometry

Parameter	Symbol	Value
Nominal Platform Height	H	300 m
Radar Wavelength	λ	0.03 m
Pixel Size	R_y	0.6 m
Baseline Length	B	1 m
Baseline Tilt	α	45°
Incidence Angle at Beam Center	θ	45°

Fig. 7 gives the true height of the simulated scene. Each ground pixel represents 0.6×0.6 meters. The tallest building in the image is eight stories tall, assuming 3 m equals one story. The building with a pyramid shaped roof reaches a total height of 21 meters and the smaller building in the foreground is four stories tall with 1 story side wings and steps leading up to the building (steps are not clearly visible from the perspective shown). In the upper corner of the image a one story and two story house is simulated with 2 m high fence posts placed along the road. The road is .3 meters below the level of the buildings, the size of a large curb. A 3 m high truck and a 2 m high car are visible in the streets as well as a 6 m high 1 pixel wide bar representing a stop light support. 6 m street lights are present between the tallest building and the houses.

For a comparison of standard phase unwrapping with multibaseline techniques, consider Fig. 8, the simulated height estimate from a single baseline using Flynn's minimum discontinuity phase unwrapping method [11]. Phase unwrapping algorithms can not determine the height of regions of the image isolated by phase discontinuities, and assume the step size is less than λ^*, the value causing a 2π phase change. When the phase is continuous, such as for the slanted roofs and the steps leading up to the building with side wings, the phase is properly unwrapped.

The first example uses the mean filter with P_{error}, the probability of having a phase wrap error, at 0.05. Figure 9 is a cross section of the scene in Fig. 7. The true height, initial estimate of the height and the estimate from the second and fourth iterations are shown. The rounding effects of the iterative spatial average are a noticeable undesirable side effect of the filter.
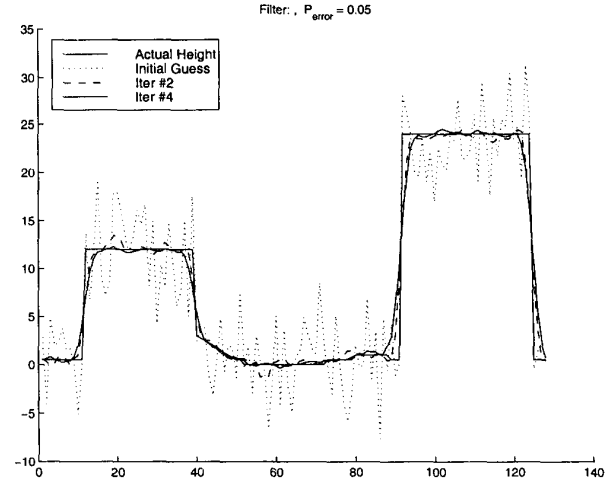

Figure 9: Cross section of the urban scene showing the iterative improvement in the height estimation using the mean filter. The baseline lengths were chosen according to Table 2.

Table 2 shows the baseline lengths for each iteration, the height λ^* which causes a 2π phase change for that baseline, $\sigma_{measured}$, the measured height accuracy for the simulation, and σ_h, the theoretical height accuracy for that baseline alone. The values for $\sigma_{measured}$ in the table are from a flat area in the scene and

Table 2: Baseline length selection for P_{error} = 0.05. The measured standard deviations represent the result of a using a 3 × 3 mean filter to eliminate errors in the height estimate.

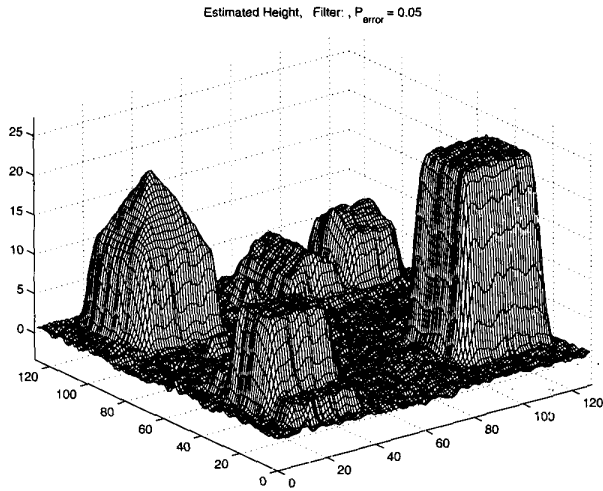| B	λ^*	$\sigma_{measured}$	σ_h
0.3	30.3	3.4	3.4
0.593	15.3	0.967	1.8
1.11	8.19	0.437	1.03
1.86	4.89	0.295	0.671
2.71	3.35	0.239	0.497

Figure 10: Final height estimate of the scene using a 3 × 3 mean filter. The resulting standard deviation is listed in Table 2.

Figure 11: The error in the final height estimate for a cross section of the urban scene using P_{error} = 0.05 and a mean filter. The largest errors occur where the mean filter has failed to maintain sharp edges, such as those found at the boundary of each building

Figure 12: Cross section of the urban scene showing the iterative improvement in the height estimation using a median filter. The baseline lengths were chosen according to Table 3.

do not account for the rounding effect of the mean filter at each step discontinuity in the image. These values are lower than the theoretical primarily because of the filtering step. The results in the table are intuitively pleasing. For each iteration the new value for λ^* is roughly half of the previous value. As the baseline length increases the spatial decorrelation increases and the percent change in λ^* correspondingly decreases. Figure 10 illustrates the result of the iterations performed using the baselines in Table 2. As expected the light poles and fence which were only one pixel wide are completely removed by the 3 ×'3 pixel mean filter. The stop light support pole is undetectable for the same reason. The sides of the buildings all have a distinct slope due to this filter. The final plot of Fig. 11 is the error in the final height estimate for the cross section shown in Fig. 9. The error is largest at the edges of the buildings where the mean filter has smoothed the jump discontinuities.

Now consider the use of a median filter on the urban scene. Figures 12 - 13 are for P_{error} = 0.05. Table 3 shows the baseline lengths used and the resulting height standard deviations, measured from each height estimate, $\sigma_{measured}$, and measured from for a given baseline, σ_h.

SUMMARY

In summary, there are many applications well-suited to low-cost SAR, including geological, archaeological, and commercial uses. That 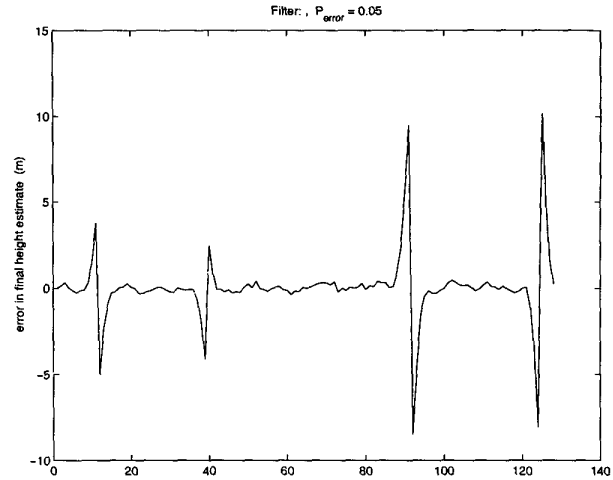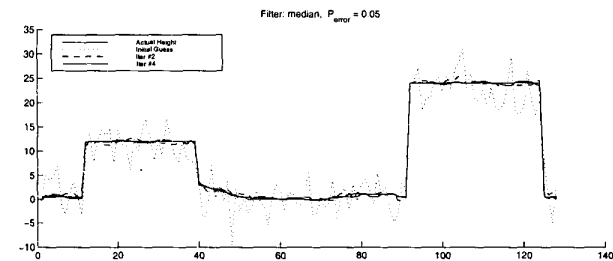such systems can produce useful images has been demonstrated by the success of YSAR. YINSAR improves on the design of YSAR in many ways and is expected to produce images which are better and more useful. We have presented new results verifying the theoretical statistics of interferograms. We have also presented a new method for combining multiple interferograms to create a height map with small error.

Table 3: Baseline length selection for P_{error} = 0.05. The measured standard deviations represent the result of a using a 3 × 3 median filter to eliminate errors in the height estimate.

B	λ^*	$\sigma_{measured}$	σ_h
0.3	30.3	3.4	3.4
0.593	15.3	0.773	1.8
1.11	8.19	0.45	1.03
1.86	4.89	0.297	0.671
2.71	3.35	0.225	0.497

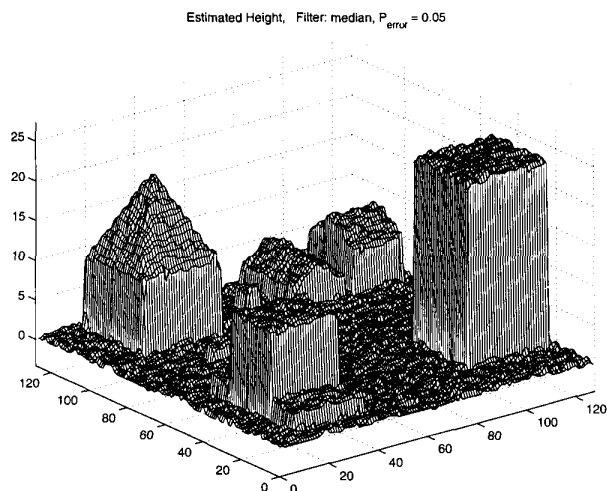Estimated Height, Filter: median, $P_{error} = 0.05$

Figure 13: Final height estimate of the scene using a 3×3 median filter. The resulting standard deviation is listed in Table 3. The median filter is edge preserving, but there are some localized errors that appear as short 'pillars' in the image. The final standard deviation in the height estimate is small enough that the curbs bordering the streets, and a small platform in front of the tallest building are visible.

ACKNOWLEDGEMENTS

References

[1] D. W. Holcomb. Shutle imaging radar and archaeological survey in china's taklamakan desert. *Journal of Field Archaeology*, 19:129–138, 1992.

[2] D. L. Evans, E. R. Stofan, T.D. Jones, and L. M. Godwin. Earth from sky. *Scientific American*, pages 70–75, Dec. 1994.

[3] F. El-Baz. Space age archaeology. *Scientific American*, pages 60–65, Aug. 1997.

[4] R. Blom, J. Zairins, N. Clapp, and G. R. Hedges. Space technology and the discovery of the lost city of ubar. *Proceedings of the 1997 IEEE Aerospace Conference*, pages 19–28, 1-8 Feb. 1997. Aspen, Colorado.

[5] H. A. Zebker and P. Rosen. On the derivation of coseismic displacement fields using differential radar inteferometry: the landers earthquake. *Proceedings of the 1994 International Geoscience and Remote Sensing Symposium*, 1:286–288, 8-12 Aug. 1994. Pasadena, CA.

[6] D. G. Thompson, D. V. Arnold, D. G. Long, G. F. Miner, and T. W. Karlinsey. Ysar: A compact, low-cost synthetic aperture radar. In *Proceedings of the 1996 International Geoscience and Remote Sensing Symposium*, pages 1892–1894, Lincoln, Nebraska, May 1996.

[7] Dieter Just and Richard Bamler. Phase statistics of interferograms with applications to synthetic aperature radar. *Applied Optics*, 1994.

[8] E. Rodriguez and J. M. Martin. Theory and design of interferometric synthetic aperture radars. *IEEE Proceedings*, 1992.

[9] Howard A. Zebker and John Villasenor. Decorrelation in interferometric radar echoes. *IEEE Transactions on Geoscience and Remote Sensing*, 1992.

[10] Fawwaz T. Ulaby, Richard K. Moore, and Adrian K. Fung. *Microwave Remote Sensing*, volume 2. Artech House Inc., 1982.

[11] Dennis C. Ghiglia and Mark D. Pritt. *Two-Dimensional Phase Unwrapping, Theory, Algorithms, and Software*. John Wiley and Sons Inc., 1998.

[12] Adam E. Robertson. Multi-baseline interferometric sar for iterative height estimation. Master's thesis, Brigham Young University, Provo, UT, December 1998.